J Mater Sci (2011) 46:1203–1210
DOI 10.1007/s10853-010-4896-3

3D printing of Al_2O_3/Cu–O interpenetrating phase composite

Reinhold Melcher · Nahum Travitzky ·
Cordt Zollfrank · Peter Greil

Received: 15 March 2010 / Accepted: 3 September 2010 / Published online: 15 September 2010

Abstract Porous alumina preforms were fabricated by indirect 3D printing using a blend of alumina and dextrin as a precursor material. The bimodal granulate powder distribution with a bed density of 0.8 g/cm^3 was increased to 1.4 g/cm^3 by overprinting. The porosity of the sintered bodies was controlled by adjusting the printing liquid to precursor powder ratio in the range of 33–44 vol%. The green bodies exhibited bending strengths between 4 and 55 MPa. An isotropic linear shrinkage of $\sim$17% was obtained due to dextrin decomposition and Al_2O_3 sintering at 1600 °C. Post-pressureless infiltration of the sintered preforms with a Cu–O alloy at 1300 °C for 1.5 h led to the formation of a dense Al_2O_3/Cu–O interpenetrating phase composite (IPC). X-ray analysis of the fabricated composites showed the presence of α-Al_2O_3, Cu and Cu_2O. $CuAl_2O_4$ spinel was not observed at the grain boundaries during HRTEM examination. The Al_2O_3/Cu–O interpenetrating phase composite revealed a fracture toughness of 5.5 ± 0.3 MPam$^{1/2}$ and a bending strength of 236 ± 32 MPa. In order to demonstrate technological capability of this approach, complex-shaped bodies were fabricated.

R. Melcher · N. Travitzky (✉) · C. Zollfrank · P. Greil
Department of Materials Science and Engineering,
Glass and Ceramics, University of Erlangen-Nuremberg,
Martensstr. 5, 91058 Erlangen, Germany
e-mail: nahum.travitzky@ww.uni-erlangen.de

N. Travitzky · P. Greil
Centre for Advanced Materials and Processes (ZMP),
Dr. Mack-Str. 81, 90762 Fuerth, Germany

Introduction

Owing to the inability of current technology related methods to produce complex-shaped ceramic parts with the desired microstructures and properties, novel additive processing techniques, such as stereolithography (SLA), selective laser sintering (SLS), fused deposition modelling (FDM), laminated object manufacturing (LOM) and three-dimensional printing (3D printing), have been emerged in last two decades, resulting in the fabrication of ceramic bodies with complex geometry [1–3].

3D printing (3DP^{TM}) is based on the principle of ink-jet printing. Two different approaches are usually discerned: direct and indirect 3D printing. In case of direct 3D printing, a dilute suspension of ceramic powder in a volatile liquid is used as ink and printed on an absorbent substrate. Repeated overprinting results in 3D green parts. In case of indirect 3D printing [4], a binder solution is locally applied on a powder layer by an ink-jet print head, causing the powder particles to bind to one another and to the printed cross-section one level below. This process is repeated until the entire part is completed. The main advantage of indirect printing is the use low viscous liquids such as water. The powder bed, however, must contain a water-soluble binder such as dextrin [5]. Indirect 3D printing was used to fabricate complex shaped ceramic structures of $TiAl_3/Al_2O_3$ [6], TiC/Ti–Cu [7], Ti_3SiC_2 [8, 9], Si–SiC [10, 11], WC/Co and TiC [12], Al_2O_3/SiO_2 [13] amongst others.

Successful use of the 3D printing, however, requires granulated powder with enhanced free-flow properties to achieve a homogeneous spreading of powder bed layers [14]. Various approaches such as application of spherical particles, bimodal particle size distribution, granulation of fine powders as well as optimisation of volume share of temporary organic compounds were used in order to increase packing density in the powder bed [1]. Furthermore, electrical [15] and magnetic [16] fields, acoustic vibration [17] and mechanical agitation [18] were employed. In case of free form powder moulding, high green density was attained by subsequent uniaxial pressing after deposition of each layer [14]. Post-isostatic pressing and melt infiltration were also applied to achieve dense materials with good mechanical properties [1–3].

Liquid metal infiltration into a porous ceramic preform is a favoured process used for the fabrication of ceramic/metal composites with interpenetrating networks [19]. Here, wetting behaviour of the ceramic matrix by the liquid metal is of high importance. If capillary forces inhibit the spontaneous or pressureless infiltration into porous ceramic matrix, external pressure must be applied for successful infiltration [20]. However, the pressureless infiltration approach is the preferred method due to increasing technical efforts during pressure-assisted infiltration.

The Al_2O_3/Cu–O system is very important in bonding processes and electronic packaging. Liquid phase formation below the melting point of pure copper and a low contact angle can be achieved by a eutectic bonding process where the presence of oxygen is crucial [21]. High contact angles of liquid copper on alumina surfaces at 1200 °C (114–170°) show non-wetting behaviour [22–25]. Oxygen partial pressure exhibited a significant influence on the surface tension of liquid copper and on its reactivity towards alumina [23, 26]. The surface energy of the liquid/vapour interface decreases with increasing oxygen partial pressure because of oxygen adsorption at the copper gas interface [27, 28]. Reactive wetting and its influence on the contact angle should be considered. $CuAlO_2$ inclusions observed in the bulk of samples prepared at $1400\,^{\circ}\mathrm{C}/p_{O_2} = 10^4$ Pa imply the solubility of Al_2O_3 in the Cu–O melt. By controlling the oxygen partial pressure and oxygen content in a copper melt the contact angle on sapphire could be varied between 22° and 125° [23]. The addition of CuO to copper resulted in a decrease of the contact angle (<90°) due to the formation of a $CuAlO_2$ at the interface [29]. Also in eutectic bonding experiments the formation $CuAlO_2$ was obtained [30]. The use of a copper/oxygen alloy close to Cu_2O resulted in decrease of the contact angle to 12° [31]. It was shown that dense Al_2O_3/Cu–O composites can be fabricated by pressureless melt infiltration of a copper alloy containing ~3.2 wt% of oxygen into porous alumina preforms prepared by uniaxial pressing [24, 25, 32, 33]. Additionally, Al_2O_3/Cu–O composites were fabricated by 3D printing technique [34]. In these studies, however, the formation of $CuAlO_2$ was not observed during examination with scanning electron microscopy (SEM) and X-ray diffraction (XRD). Although presented results, a grain boundary formation in these composites has not been studied systematically by means of a high-resolution transmission electron microscopy. Moreover, the influence of the printing conditions on the porosity of performs prior to pressureless infiltration with Cu–O alloy have not been investigated.

The purpose of this work was to fabricate dense Al_2O_3/Cu–O composites by an indirect 3D printing technique. The specific objectives were to: (a) control the porosity of the printed Al_2O_3 preforms by variation of printing conditions; (b) fabricate dense materials by post-pressureless vacuum infiltration with Cu–O alloy; and (c) evaluate phase composition, microstructure and mechanical properties of such composites.

Experimental

Sample preparation: powder processing and 3D printing

Al_2O_3 powder with an average particle size of 0.8 µm (CT 3000 SG, Almatis, Ludwigshafen, Germany) and potato dextrin powder ($C_6H_{10}O_5$) with an average particle size of 115 µm (Kartoffel-Dextrin Superior gelb-mittel F, Suedstaerke, Schrobenhausen, Germany) were used. Alumina and dextrin powders were blended by dissolving a dispersant (Darvan C, R.T. Vanderbilt, Norwalk/CT, USA) and dextrin (1 and 6 wt%, respectively, referring to alumina) in distilled water at 60 °C and then alumina powder was added. The mixture was tumbled in a 2 L-polyethylene bottle with Al_2O_3 grinding balls with a diameter of 20 mm for 24 h (Reax 20, Heidolph, Schwabach, Germany) and then freeze-dried (Delta 2-24, Christ, Osterode/Harz, Germany). The dry mixture was jar-milled for at least 24 h and sieved through 150 µm mesh. Particle size distribution of granulate powders prepared were measured by laser granulometric analysis in an air stream (Mastersizer 2000/Scirocco 2000, Malvern Instruments, Malvern, GB). Alumina raw material was suspended and measured in double distilled water. The expected porosity of the granulate powder was calculated (MIX10/MixConv 3.0, Dinger & Funk, Dinger Ceramic Consulting Services, Clemson/SC, USA) using the Dinger–Funk equation [34–36]. The density of the spread powder granulate bed was calculated from the weight and the volume corresponding to 50 layers with a thickness of 100 µm. Mean density was determined from weight and volume of the granulate powder using a measuring glass cylinder. Tamped density was measured using a jolting volumeter (STAV 2003, JEL Engelsmann, Ludwigshafen, Germany). Five strokes were applied. Green density was determined from weight and volume of printed and dried samples.

The part geometry was designed using a conventional CAD-program (Solid Edge v.17/academic, PLM Solutions,

Table 1 Composition of printing liquid

Content (wt%)	Chemical name	Trade name	Supplier
94.5	Water	2× Distilled	
2.5	Glycerin	Anhydrous, p.a.	Merck, Darmstadt, Germany
1.0	Polyethylene glycol	PEG 300	Sigma-Aldrich, Steinheim, Germany
1.0	Fatty alcohol polyalkylene glycol ether	Propetal 160	Zschimmer & Schwarz, Lahnstein/Ruhr, Germany
0.5	Polyvinyl alcohol	Mowiol 4-88	Kuraray Specialties Europe, Frankfurt/Main, Germany
0.5	Potassium sorbate	p.a.	Fluka Chemie, Buchs, Switzerland

Huntsville/AL, USA). 3D printing was performed on a Z-printer 310 (Z-Corporation, Burlington/MA, USA) using a water-based printer solution, Table 1. Bar-shaped samples (60 × 7.7 × 6 mm^3) for the examination of the influence of binding liquid saturation, crucible-shaped objects (120 × 50 × 20 mm^3) for the purpose of infiltration and cylindrical specimens (length: 26 mm, ∅: 10 mm) being orientated in *x*-, *y*- and *z*-direction for dilatometric examination were printed. Layer thickness was set to 100 μm for all objects and the binding liquid saturation was adjusted to 0.35 g/cm^3. Oriented bar-shaped specimens were printed using varied binding liquid saturations of 0.14, 0.21, 0.28 and 0.35 g/cm^3, respectively. Orientations are defined as follows: *x* moving direction of carriage, *y* moving direction of print head, *z* moving direction of pistons, Fig. 1. After being dried in air at room temperature for 24 h, the printed objects were removed and cleaned from the unbound powder bed.

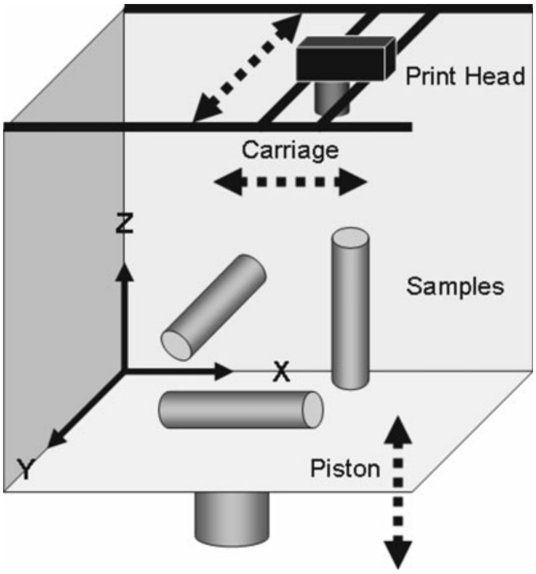

Fig. 1 Sample orientation within the building chamber of 3D-printer

Sintering and melt infiltration

The sintering was investigated on the cylindrical samples printed in *x*-, *y*- and *z*-direction in air with a flow rate of 6 mL/min (dilatometer Dil-402E, Netzsch, Selb, Germany). Samples with non-cylindrical shape were heat treated in a resistance heated furnace in air according to the dilatometric data as follows: 25–600 °C at 10 °C/min, 600–1100 °C at 20 °C/min, 1100–1600 °C at 5 °C/min. The samples were held at the maximum temperature of 1600 °C for 2 h. The cooling rate down to room temperature was 10 °C/min.

For the melt infiltration, Cu and Cu_2O powders (both Strem Chemicals, Newburyport/MA, USA) were dry-mixed at the ratio of 72:28 wt% [24]. The mixture was placed into the 3D printed and sintered alumina crucible (printed with 0.35 g/cm^3 printing liquid saturation) and heated to 1300 °C in a resistance-heated furnace in vacuum (<10 Pa). Exposure time at maximum temperature was 1.5 h. Heating and cooling rates were 5 °C/min. The infiltrated crucible was cut into bars for microstructure analysis and mechanical properties evaluation. Complex parts were melt-infiltrated in a dense alumina crucible using a wick prepared from printed porous alumina under the same experimental conditions.

Microstructure and phase composition

The open porosity of green and sintered specimens was measured by Hg-porosimetry (Pascal 140, Thermo Electron, Rodano/Milan, Italy). Total porosity was calculated by multiplication of bulk density (BD) and total cumulative volume (TCV), where TCV equals to measured pore volume divided by weight of sample. Apparent density was calculated according to $1/((1/\mathrm{BD}) - \mathrm{TCV})$.

The phase analysis of the infiltrated samples was conducted by XRD (Kristalloflex D 500, Siemens, Karlsruhe, Germany) using monochromatic Cu-Kα radiation at a scan rate of 0.75°/min over a 2θ range of 20°–70°.

Sintered and infiltrated samples were metallographically polished and examined by SEM (Quanta 200, FEI, Czech Republic). Grain boundaries of Al_2O_3/Cu and Al_2O_3/Cu_2O

specimens were investigated in a high-resolution transmission electron microscope (HRTEM, Philips CM300-UT, Eindhoven, The Netherlands) operated at 300 kV. The fabricated Al_2O_3/Cu–O composites were sectioned into plates with a thickness of 0.7 mm using a diamond-coated circular saw. Discs with a diameter of ~3 mm were obtained using an ultrasonic disc cutter (Gatan, model 601, Munich, Germany). One side of the discs was polished using various diamond laps and cloths. The samples were turned and mechanically ground to a thickness of ~40 µm. Further thinning and polishing was performed using a dimple grinder (Gatan, model 656, Pleasanton, USA) followed by ion-beam thinning with a precise ion polishing system (PIPS, Gatan, model 691, Ar, Pleasanton, USA) operated at 4 kV at an angle of 5°.

Mechanical properties

Bending strength and fracture toughness of sintered preforms and infiltrated bars (both $36 \times 3.9 \times 2.7$ mm^3) obtained from the crucibles were measured by 4-point bending method using spans of 10 and 20 mm. Testing bars with different layer orientation were prepared in order to be loaded in the three different modes regarding layer stacking direction, Fig. 2. The tensile surfaces of the samples were polished to a 6 µm diamond finish prior to bending. The tests were performed using a testing machine (Exakt 6000EA, Exakt, Norderstedt, Germany) with a crosshead speed of 10 µm/s.

Fracture toughness of preforms and infiltrated samples was determined using single-edge-V-notched beam method (SEVNB) [37]. Precracking was performed by low speed diamond sawing and consecutive razor blade notching with 3 µm diamond abrasive paste. Precrack length was adjusted to ~0.3 of sample height (DIN 51109). Average values of bending strength and fracture toughness were calculated from at least 10 measurements.

Young's modulus of preforms and infiltrated samples was calculated from the longitudinal sound-propagation velocity measurements using the impulse excitation technique (Buzz-o-Sonic, BuzzMac Software, Glendale, USA) [38].

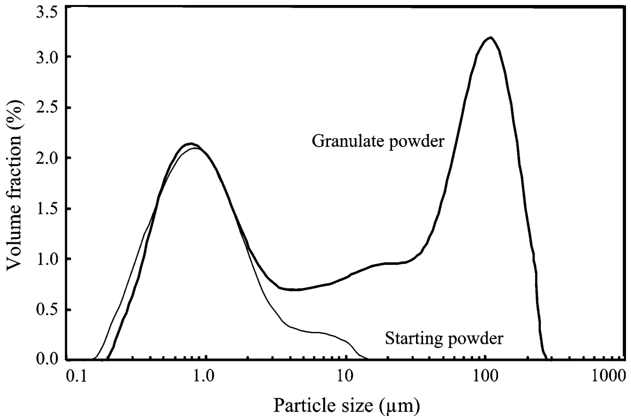

Fig. 3 Particle size distribution of granulate powder prepared with alumina and dextrin (prior to sieving) and alumina starting material (raw material volume fraction was scaled to fit first peak at 0.8 µm)

Vickers' hardness (Zwick 3212, Zwick, Ulm, Germany) of the infiltrated samples was measured at a load of 98.1 N applied for 15 s. Average values of hardness were calculated from at least twenty indentations.

Results and discussion

3D printing

The alumina starting material exhibited a monomodal distribution with a maximum at 0.8 µm, Fig. 3. Particle size analysis of the granulate powder showed a bimodal distribution with maxima at 0.8 and 112 µm indicating that the granulate consisted of both fractions of primary as well as secondary particles. Improved spreading into the building chamber was obtained by the use of granulated powder. Powder bed density (0.8 g/cm^3) which was lower than mean density (1.0 g/cm^3) showed that compaction using the rotating feed roller of the 3D printer was not observed. The increase of the density in the printed material (1.4 g/cm^3, green body) showed that the application of the printing liquid led to densification by a factor of 1.75. Apparent density (2.8 g/cm^3, skeleton density) showed a porosity of 22 vol% within the struts. The relatively high value might

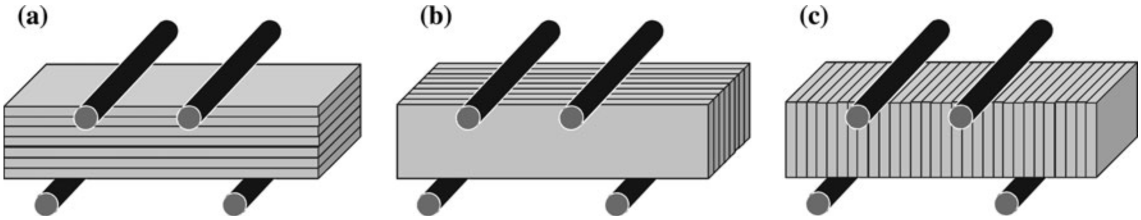

Fig. 2 Sample loading modes

Table 2 Porosity of green and sintered samples depending on printing liquid saturation

Printing liquid saturation (g/cm^3)	Porosity green (vol%)	Porosity sintered (vol%)
0.14	n.a.	43.8
0.21	56.4	38.5
0.28	53.1	35.9
0.35	52.0	33.0

be explained by the formation of a thin film of slurry during contact with the printing liquid, which might lead to a local rearrangement of the particles.

Sintering and melt infiltration

Removal of binder by oxidation was completed at 600 °C without significant dimensional changes. Sintering started at 1100 °C and completed after 5 h at 1600 °C. After sintering a linear shrinkage of 17.4, 16.9 and 17.0 % was measured for samples being oriented in *x*-, *y*- and *z*-direction, respectively. As a result, isotropic shrinkage of the printed alumina after sintering can be assumed. Porosity data of samples printed with different printing liquid saturations is given in Table 2. Samples printed with 0.14 g/cm^3 could not be measured in the green state due to their low mechanical stability under Hg-pressure. Pore size distribution is similar for all samples with two maxima at 0.14 and 30 µm, whereas the pore size distribution in the sintered state is monomodal with one maximum at 25 µm. Pressureless infiltration of Cu–O alloy into Al_2O_3 preforms led to the formation of a nearly dense Al_2O_3/Cu–O composite with a homogeneous interpenetrating microstructure. The fracture surface of the fabricated composites exhibited sharp edges due to plastic deformation of the metal phase. Obtained results are similar to these reported in reference [39].

X-ray diffraction (XRD) revealed Al_2O_3, Cu and Cu_2O as the only phases to constitute the present composite material. HRTEM examination of Cu/Al_2O_3 and Cu_2O/Al_2O_3 interfaces showed grain boundaries without any reaction products located at the interfaces, Fig. 4.

The presence of α-Al_2O_3, Cu and Cu_2O detected by SEM, TEM and XRD analyses is in good agreement also with published results [24]. In contrast to the dissolution of the Cu_2O cuprite phase in copper and subsequent spinel formation [40], however, the presence of cuprite phase on the interface between alumina and copper [24] was demonstrated in our case. The formation of a thin $CuAlO_2$ layer at the interface of alumina and preoxidized copper was observed by transmission electron microscopy investigation [27, 30], whereas in the present work the occurrence of $CuAlO_2$ spinel could not be confirmed, Fig. 4. As a result of the decrease of the oxygen partial pressure with increasing temperature below $4.9 \cdot 10^{-18}$ Pa at 1200 °C detectable reaction products were absent from the interfaces [22]. In previous studies it was shown that Al_2O_3 is stable in Cu at the low oxygen concentrations during infiltration [23, 26]. The adsorption of a Cu–O complex on the Al_2O_3 surface might play a key role in promotion of wettability. Possible formation of $CuAlO_2$ and dissolution of Al_2O_3 in the Cu melt might also influence the contact angle. In the presence of Al_2O_3 the formation of $CuAlO_2$ and $CuAl_2O_4$ from Cu–O melts might also occur. Al_2O_3 solubility increases with oxygen content in the copper. As a result the growth of $CuAlO_2$ at the interface can be expected only below a certain temperature depending on oxygen partial pressure [23]. In a recent study, a model for the adsorption of oxygen at metal/oxide interfaces was proposed [25]: oxygen in the melt is bound in a Me–O complex. Upon adsorption at the oxide surface, these complexes are oriented and located in such a way that the metal ion faces the oxide surface and is situated near a surface oxygen ion. A monolayer of metal oxide is

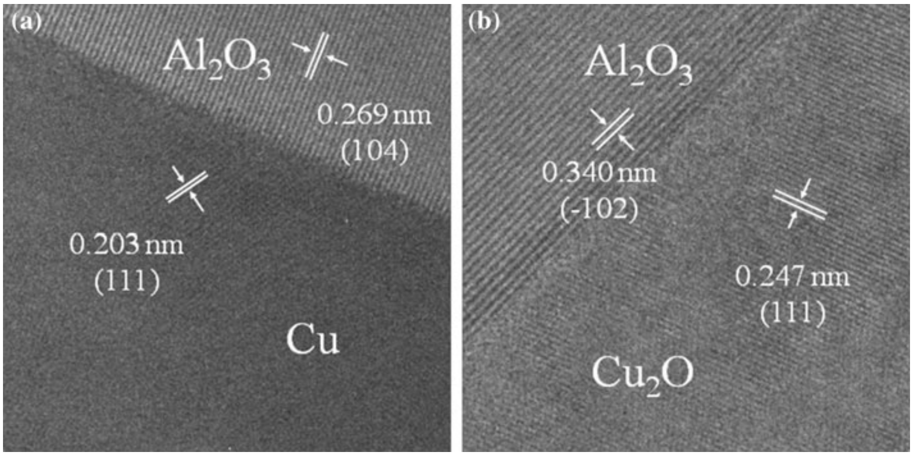

Fig. 4 HRTEM micrographs of **a** Al_2O_3/Cu, **b** Al_2O_3/Cu_2O interfaces

thereby formed at the interface, which decreases the solid/liquid interfacial energy. It was previously suggested that thermodynamically controlled wetting is not always readily achieved in metal-oxygen systems [23]. Kinetically controlled wetting and time-dependent effects are expected if one or more of the following conditions prevail: (a) time required for oxygen diffusion through the drop is long compared to the length of the experiment; (b) the equilibrium concentration of oxygen in the melt is high, and the buffer capacity of the gas phase is limited—this situation is frequently encountered in the p_{O_2} range where no buffer gas mixtures are used and (c) interfacial reactions are slow compared to the time scale of the experiment. In the observed time-dependent effects the thermodynamic equilibrium between the gas phase and the copper melt could not be attained [23]. A time dependence of the wetting angle for Cu melts containing ~2.6 wt% of oxygen at 1300 °C, similar to the conditions used in the present work, might result in a chemical non-equilibrium with the gas phase. Therefore, the solubility of Al_2O_3 was insufficient for $CuAlO_2$ formation. Samples produced at those low partial pressures do not have a sufficient oxygen content of the copper melt to allow the interfacial layer to grow. In contrast to the current work, the formation of $CuAlO_2$ was shown at higher oxygen partial pressures [23].

Mechanical properties

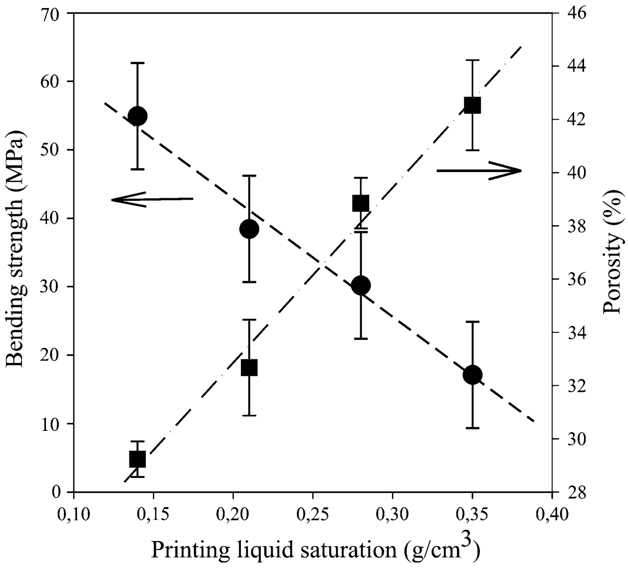

Fig. 5 Correlation of printing liquid saturation, bending strength and porosity in sintered state

Table 3 Mechanical properties of sintered Al_2O_3 preforms (0.35 g/cm^3 printing liquid saturation)

Al_2O_3 preform	Mode A	Mode B	Mode C
4-Point bending strength (MPa)	56 ± 3	53 ± 3	19 ± 2
Young's modulus (GPa)	113 ± 5	93 ± 4	92 ± 13
Fracture toughness K_{Ic} (MPam$^{1/2}$)	1.6 ± 0.1	1.8 ± 0.1	0.5 ± 0.1

Table 4 Mechanical properties of Al_2O_3/Cu–O composites

Al_2O_3/Cu–O Composite	Mode A	Mode B	Mode C
4-Point bending strength (MPa)	236 ± 32	245 ± 43	222 ± 15
Young's modulus (GPa)	204 ± 8	198 ± 9	194 ± 9
Fracture toughness, K_{Ic} (MPam$^{1/2}$)	5.5 ± 0.3	5.6 ± 0.8	5.0 ± 1.0
Vickers' hardness HV_{10} (GPa)	2.5 ± 0.1	2.4 ± 0.3	2.4 ± 0.5

Figure 5 shows the dependence of bending strength for mode A (see Fig. 2) and porosity of the sintered samples on printing liquid saturation. An increase of the printing liquid saturation led to a linear decrease of porosity from 42 to 32 vol% and an increase in bending strength from 5 to 57 MPa. Mechanical properties of the preforms and the Al_2O_3/Cu–O composites are summarized in Tables 3 and 4. Bending strengths of 56 ± 3 and 53 ± 3 MPa were evaluated for the modes A and B, respectively, of the sintered preforms, whereas the bending strength of preforms with crack induction parallel to layers attained 19 ± 2 MPa. In contrast, bending strength in the infiltrated state attained 222–245 MPa, whereby the differences between the loading modes can be neglected considering the standard deviation. Sintered Al_2O_3 preforms exhibit a fracture toughness of 1.6 ± 0.1 and 1.8 ± 0.1 MPam$^{1/2}$ for loading modes A and B, respectively. In the case of mode C where crack induction was parallel to layer planes fracture toughness attained 0.5 ± 0.1 MPam$^{1/2}$. Fracture toughness of the as-fabricated Al_2O_3/Cu–O composite attained 5.0–5.6 MPam$^{1/2}$, whereby standard deviation levels the differences between loading modes. Crack bridging by the metal phase may control fracture toughness of this type of composite [41]. Crack deflection and/or process zone shielding are additional possible mechanisms. In many cases it was observed that the two halves of broken specimens were still sticking together after load drop. The hardness of the Al_2O_3/Cu–O composite attained 2.4–2.5 GPa depending on orientation of tested surface. The low hardness is typical for composites with large metal contents, apparently due to the low fraction of the hard alumina phase forming a relatively weak network. As a consequence, mutual sliding of alumina grains takes place and plastic flow of the metal phase is enabled. This is confirmed by chipping that was also observed. Young's moduli of preforms and infiltrated samples attained average values of 92–113 GPa and 194–204 GPa, respectively, depending on testing mode. Differences can be neglected in

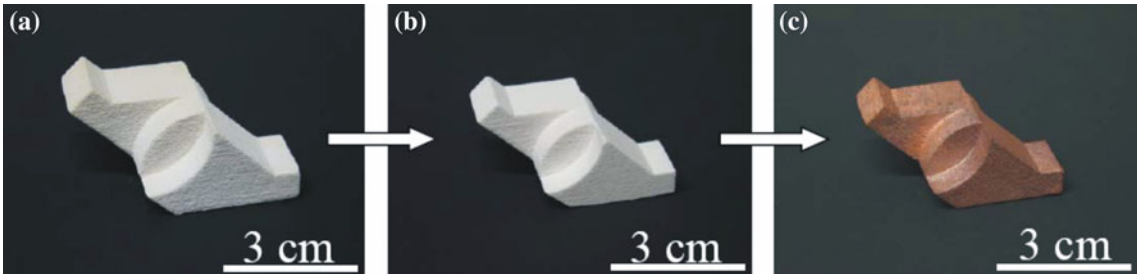

Fig. 6 Complex-shaped Al_2O_3/Cu–O body fabricated by 3D printing: **a** as printed Al_2O_3/dextrin preform; **b** sintered Al_2O_3 preform (linear shrinkage ~17%); **c** Cu–O infiltrated Al_2O_3/Cu–O

sintered as well as infiltrated state considering the standard deviation.

In order to demonstrate the capability of the 3D printing complex shaped bodies were fabricated. The automatic generation of the part via a 3D-CAD file is shown in Fig. 6. All details of the part can be maintained. Mechanical properties of the printed and sintered body are sufficient to handle it safely during post-infiltration. During infiltration with Cu–O alloy, the geometrical shape of the part is preserved and no further dimensional change takes place.

Conclusions

Complex shaped alumina preforms were fabricated by indirect 3D printing. Total porosity was controlled over printing liquid saturation in the range of 33–44 vol% after sintering at 1600 °C. Dense Al_2O_3/Cu–O composites were fabricated by pressureless melt infiltration of those preforms with Cu–Cu_2O alloy containing 3.2 wt% of oxygen at 1300 °C under vacuum. XRD, SEM as well as TEM examination did not reveal any formation of $CuAlO_2$ spinel in the composite. Mechanical properties in the infiltrated state were found to be largely isotropic despite the layered fabrication. The fabricated composite exhibits a fracture toughness of up to 5.6 $MPam^{1/2}$, bending strength of up to 245 MPa, Young's modulus of up to 204 GPa and Vickers' hardness of ~2.5 GPa.

References

1. Beaman JJ, Barlow JW, Bourell DL, Crawford RH, Marcus HL, McAlea KP (1997) Solid freeform fabrication: a new direction in manufacturing. Springer Verlag, Heidelberg, New York
2. Cima MJ, Yoo J, Khanuja S, Rynerson M, Nammour D, Giritlioglu B, Grau J, Sachs EM (1995) In: Proceedings of the solid freeform fabrication symposium, Austin, TX, p 479
3. Goetzel CG, Groza J (1998) Metals handbook ASM handbook, vol 7 powder metal technologies and applications. ASM International, Materials Park
4. Cima M, Sachs E, Fan T, Bredt JF, Michaels SP, Khanuja S, Lauder A, Lee S-JJ, Brancazio D, Curodeau A, Tuerck H (1995) US Patent No. 5,387,380
5. Melcher R, Zhang W, Travitzky N, Greil P (2006) Ceram Forum Int 83(13):18
6. Yin X, Travitzky N, Melcher R, Greil P (2006) Int J Mater Res 97(5):492
7. Rambo CR, Travitzky N, Zimmermann K, Greil P (2005) Mater Lett 59:1028
8. Dcosta DJ, Sun W, Lin F, El-Raghy T (2002) J Mater Proc Technol 127:352
9. Sun W, Dcosta DJ, Lin F, El-Raghy T (2002) J Mater Proc Technol 127:343
10. Travitzky N, Zimmermann K, Melcher R, Greil P (2006) In: Bansal NP, Singh JP, Kriven WM (eds) Advances in ceramic matrix composites XI. American Ceramic Society, Westerville, OH, p 37
11. Moon J, Caballero AC, Hozer L, Chiang Y-M, Cima JC (2001) Mater Sci Eng A 298(12):110
12. Michaels S, Sachs EM, Cima MJ (1994) In: Lall C (ed) Advanced processing techniques. Metal Powder Industries Federation, Princeton, NJ, p 103
13. Sachs E, Cima M, Bredt J, Curodeau A, Fan T, Brancazio D (1992) Manufacturing review 5(2):117
14. Paul BK, Baskaran S (1996) J Mater Proc Technol 61(1–2):168
15. Melvin LS, Beaman JJ (1991) In: Proceedings of the solid freeform fabrication symposium, Austin, TX, p 171
16. Melvin LS, Beaman JJ (1991) In: Proceedings of the solid freeform fabrication symposium, Austin, TX, p 118
17. Sachs EM (2000) US Patent 6,036,777
18. Bunnel DE, Das S, Bourell DL, Beaman JB, Marcus HL (1995) In: Proceedings of the solid freeform fabrication symposium, Austin, TX, p 440
19. Lange FF, Velamakanni BV, Evans AG (1990) J Am Ceram Soc 73(2):388
20. Mortensen A (2000) In: Clyne TW (ed) Metal matrix composites. Pergamon, Oxford, p 521
21. Yoshino Y (1998) J Am Ceram Soc 72(8):1322
22. Bahraini M, Weber L, Narciso J, Mortensen A (2005) J Mater Sci 40:2487. doi:10.1007/s10853-005-1980-1
23. Diemer M, Neubrand A, Trumble KP, Rödel J (1999) J Am Ceram Soc 82(10):2825
24. Travitzky NA, Shlayen A (1998) Mater Sci Eng A 244:154
25. Naidich JV (1981) Prog Surf Membr Sci 14:354
26. Zhang W, Smith JR, Evans AG (2002) Acta Mater 50:3803
27. Ghetta V, Fouletier J, Chatain D (1996) Acta Mater 44(5):1927
28. O'Brien TE, Chaklader ACD (1974) J Am Ceram Soc 57(8):329
29. Chaklader ACD, Armstrong AM, Misra SK (1968) J Am Ceram Soc 51:630
30. Beraud C, Courbiere M, Esnouf C, Juve D, Treheux D (1989) J Mater Sci 24:4545. doi:10.1007/BF00544543

31. Meier A, Baldwin MD, Chidambaram PR, Edwards GR (1995) Mater Sci Eng A 196:111
32. Travitzky NA (1998) Mater Lett 36:114
33. Halden FA, Kingery WD (1995) J Phys Chem 59:557
34. Dinger DR, Funk JE (1990) Ceram Bul 69(1):58
35. Dinger DR, Funk JE (1990) Ceram Bul 69(2):204
36. Funk JE, Dinger DR (1994) Predictive process control of crowded particulate suspensions. Kluwer Academic Publishers, Boston
37. Munz D, Fett T (2001) Ceramics. Springer, Berlin
38. Radovic M, Lara-Curzio E, Riester L (2004) Mater Sci Eng A 368:56
39. Melcher R, Martins S, Travitzky N, Greil P (2006) Mater Lett 60:572
40. Gonzalez EJ, Trumble KP (1996) J Am Ceram Soc 79(1):114
41. Prielipp H, Knechtel M, Claussen N, Streiffer SK, Mullejans H, Ruehle M (1995) Mater Sci Eng A 197:19